

Review

Rare-Earth Tantalates and Niobates Single Crystals: Promising Scintillators and Laser Materials

Renqin Dou ¹, Qingli Zhang ^{1,*}, Jinyun Gao ¹, Yuanzhi Chen ^{1,2}, Shoujun Ding ^{1,2}, Fang Peng ¹, Wenpeng Liu ¹ and Dunlu Sun ¹

¹ The Key Laboratory of Photonic Devices and Materials, Anhui Institute of Optics and Fine Mechanics, Chinese Academy of Sciences, Hefei 230031, China; drq0564@126.com (R.D.); jygao1985@gmail.com (J.G.); yzchan@mail.ustc.edu.cn (Y.C.); dsjqy@mail.ustc.edu.cn (S.D.); pf23208@163.com (F.P.); wpli@aiiofm.ac.cn (W.L.); dlsun@aiiofm.ac.cn (D.S.)

² Science Island Branch of Graduate School, University of Science and Technology of China, Hefei 230026, China

* Correspondence: zql@aiiofm.ac.cn; Tel./Fax: +86-551-6559-1039

Received: 11 December 2017; Accepted: 28 December 2017; Published: 24 January 2018

Abstract: Rare-earth tantalates, with high density and monoclinic structure, and niobates with monoclinic structure have been paid great attention as potential optical materials. In the last decade, we focused on the crystal growth technology of rare-earth tantalates and niobates and studied their luminescence and physical properties. A series of rare-earth tantalates and niobates crystals have been grown by the Czochralski method successfully. In this work, we summarize the research results on the crystal growth, scintillation, and laser properties of them, including the absorption and emission spectra, spectral parameters, energy levels structure, and so on. Most of the tantalates and niobates exhibit excellent luminescent properties, rich physical properties, and good chemical stability, indicating that they are potential outstanding scintillators and laser materials.

Keywords: rare-earth tantalates; rare-earth niobates; scintillator crystals; laser crystals

1. Introduction

In recent decades, rare-earth tantalates and niobates have been paid great attention due to their rich physical properties and good chemical stability [1–4]. Commonly, chemical forms of the rare-earth tantalates and niobates are written as REBO₄, RE₃BO₇, REB₃O₉, REB₅O₁₄, and REB₇O₁₉, where RE means rare earth ions, and B are Ta or Nb elements [5,6]. Orthotantalates and orthoniobates REBO₄ belong to the fergusonite structure and have been reported extensively [7–9]. By comparison and analysis, REBO₄ exhibited excellent luminescent properties [10]. Moreover, RE ions can be substituted easily by other trivalent ions to realize characteristic fluorescence emission, from the ultraviolet to the infrared region [11]. With the change of RE ions radius, there are three different structures. With the larger ionic radii (La-Pr), they crystallize in structure $P2_1/c$ (C_{2h}^5 , #14, $Z = 4$), while with intermediate ionic radii (Nd-Tb) they exhibit the fergusonite M-type structure $I2/a$ (C_{2h}^6 , #15, $Z = 4$). Furthermore, with the smaller ionic radii (Dy-Lu) they present the fergusonite M'-type structure $P2/a$ (C_{2h}^4 , #13, $Z = 2$) [11–13].

At present, with an increasing demand in dense, fast, and bright scintillators for high-energy physics, medical diagnostics, and security screening devices, the scintillation characteristics of the lanthanide orthotantalates and orthoniobates REBO₄ have been widely investigated for the development of new scintillator materials [9,14,15]. Among REBO₄ materials, RETaO₄ are favorable for the registration of high-energy particles due to their extremely high density ranging from 7.8 g/cm³ for LaTaO₄ to 9.75 g/cm³ for LuTaO₄, which are partly higher than the density of Bi₄Ge₃O₁₂ (BGO 7.1 g/cm³) and PbWO₄ (PWO 8.28 g/cm³). Normally, the rare-earth tantalates are

studied systematically with polycrystalline samples produced by solid-state reaction [9]. Although the optical absorption and luminescence of RETaO_4 crystals are described, the crystal size is too small, only $7 \text{ mm} \times 7 \text{ mm} \times 1 \text{ mm}$ [10]. It is urgent to develop the growth technology of large RETaO_4 crystals for the device application. Recently, our group has made great progress in the Cz growth of large-size tantalite crystals and obtained big and fine GdTaO_4 single crystals, which would promote the growth and practical application of RETaO_4 [16].

In addition, REBO_4 have been considered appropriately as host matrices and have also attracted wide interests as potential rare earth-doped laser hosts [17]. They belong to monoclinic system and have large crystal field energy. The active ions occupy the site with C_2 symmetry (RE sites), which is advantageous to remove the parity-forbidden rule of $f-f$ transition. Therefore, it is beneficial for the realization of new emission and tunable wavelength. Additionally, their mechanical and thermal properties are also sufficient for laser applications.

Recently, on the one hand, our group have finished a lot of research works on scintillation characteristics of RETaO_4 , such as GdTaO_4 , Tb:GdTaO_4 , LuTaO_4 , Nd:LuTaO_4 , and so on. The luminescence results indicate that GdTaO_4 and Nd:LuTaO_4 are the promising scintillator candidates. On the other hand, the emission spectra of active ions (Yb, Nd, Er, Ho) doped GdBO_4 , YBO_4 , and mixed GdYBO_4 crystals show that they can be used as the new materials for visible, near, and middle infrared lasers. Meanwhile, near infrared lasers are realized on the Yb and Nd-doped ReBO_4 successfully.

2. Experiments

2.1. Polycrystalline Synthesis

In this paper, LuTaO_4 and Nd-doped LuTaO_4 series samples were prepared by solid-state reaction method using Lu_2O_3 (99.99%), Ta_2O_5 (99.99%), and Nd_2O_3 (99.999%) as starting materials. First, the raw materials were weighed accurately according to the appropriate stoichiometric ratio and then mixed and ground in a mortar. The mixed powders were then heated to $1500 \text{ }^\circ\text{C}$ at a heat rate of approximately $2.3 \text{ }^\circ\text{C}/\text{min}$ and calcined at $1500 \text{ }^\circ\text{C}$ for 24 h. Finally, the calcined samples were slowly cooled to room temperature and then carefully ground for the measurements.

2.2. Single Crystal Growth

All of the crystals, mentioned in the text, were grown by the Czochralski (Cz) method. Raw materials, with high purity ($>4 \text{ N}$), were weighed stoichiometrically, mixed thoroughly, and then pressed into disks. The disks were put into an iridium crucible and melted in a JGD-60 furnace with an automatic diameter controlled system. Using a seed, the crystals were grown in nitrogen atmosphere with a rotation speed of $3.0\text{--}10.0 \text{ rpm}$ and pulling rate of $0.35\text{--}1 \text{ mm/h}$. The growth process of all crystals is similar. The as-grown crystals and some samples are shown in Figure 1.

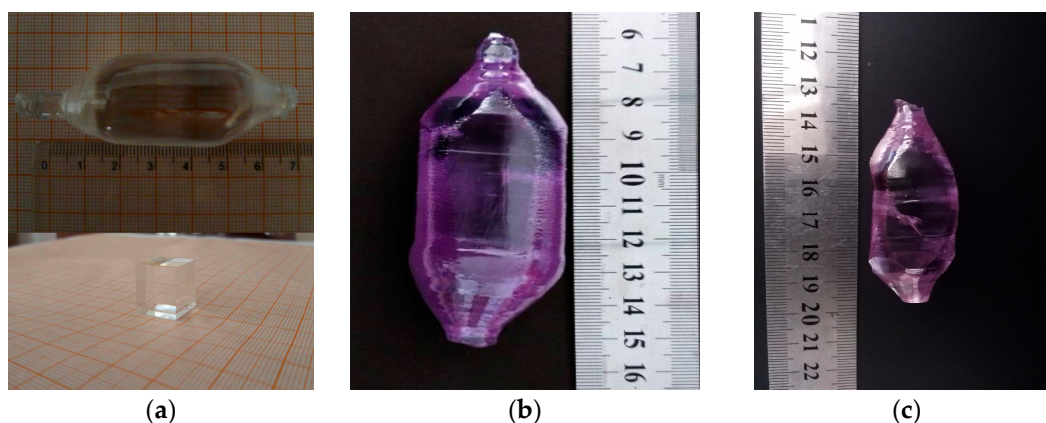


Figure 1. Cont.

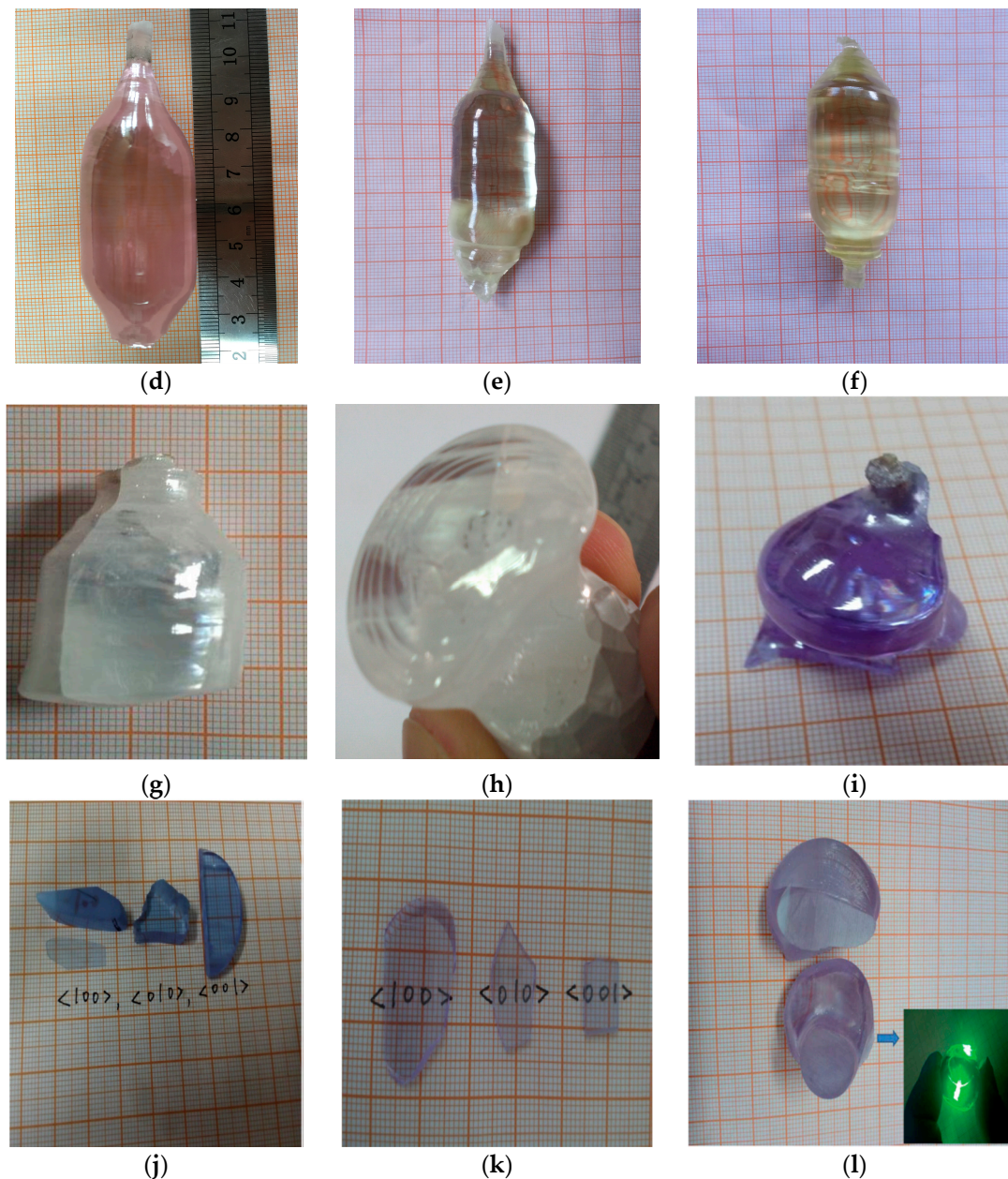


Figure 1. Photographs of the as-grown crystals: (a) GdTaO_4 ; (b) Nd:GdTaO_4 ; (c) Nd:GdYTaO_4 ; (d) Er:GdTaO_4 ; (e) Tm,Ho:GdYTaO_4 ; (f) Yb,Ho:GdYTaO_4 ; (g) Yb:GdNbO_4 ; (h) Yb:YNbO_4 ; (i) Nd:GdNbO_4 ; (j) Nd:YNbO_4 ; (k) Nd:GdYNbO_4 ; and (l) Nd:GdLaNbO_4 .

2.3. Crystal Structure and Chemical Etching

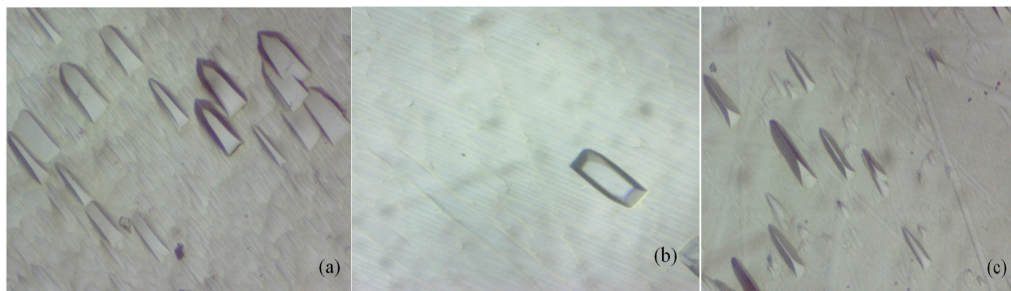
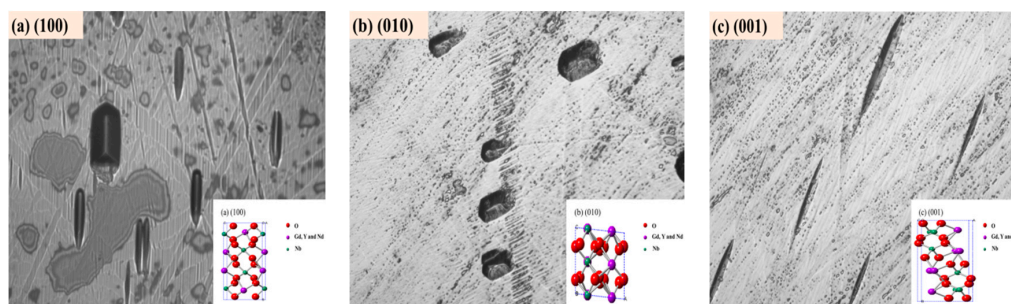
Generally, crystal structure can be determined by X-ray diffraction (XRD). The XRD patterns of as-grown crystals are measured with a X'pert PRO X-ray diffractometer (PANalytical, Almelo, The Netherlands) employing $\text{Cu K}\alpha$ radiation ($\lambda = 1.540598 \text{ \AA}$). The diffraction data are recorded in the 2θ range of 10° – 90° with a scan step of 0.033° . The structural parameters of above crystals are obtained by fitting the XRD data with the Rietveld refinement method. The structural parameters of pure GdTaO_4 or GdNbO_4 are taken as the initial values, the background function, lattice parameters, atomic coordinates, and isotropic temperature factors are refined with the software GSAS. The refinement results of cell parameters are shown in Table 1. Since the ionic radius of doped ions is smaller than that of the replaced ions, there is a slight decrease in the cell volume and density.

Table 1. Lattice parameters of as-grown crystals.

Crystal	<i>a</i> (Å)	<i>b</i> (Å)	<i>c</i> (Å)	β (°)	ρ (Å ³)	<i>V</i> (g cm ³)	<i>R_p</i> %	<i>R_{up}</i> %
GdTaO ₄	5.41	11.05	5.07	95.58	8.83	302.56	-	-
Nd:GdTaO ₄	5.40	11.06	5.08	95.61	8.89	302.09	4.3	6.24
Nd:GdYTaO ₄	5.38	11.04	5.08	95.58	8.42	300.25	9.9	7.34
Er:GdTaO ₄	5.41	11.06	5.09	95.61	8.79	302.70	5.20	7.20
Tm,Ho:GdYTaO ₄	5.39	11.03	5.08	95.61	8.595	300.43	8.91	6.22
Yb,Ho:GdYTaO ₄	5.39	11.04	5.08	95.60	8.602	300.68	2.92	1.11
Yb:GdNbO ₄	5.36	11.07	5.10	94.57	7.140	301.459	4.58	6.26
Nd:GdNbO ₄	5.38	11.09	5.11	94.56	6.875	303.410	4.14	5.44
Nd:YNbO ₄	7.041	10.952	5.301	94.56	5.568	299.640	6.70	8.75
Nd:GdYNbO ₄	5.350	11.050	5.090	94.56	6.525	300.312	4.04	5.28
Nd:GdLaNbO ₄	5.381	11.112	5.111	94.56	6.791	304.694	5.86	4.20

It is very meaningful to research the crystal defects in the as-grown crystal. The crystal with defects may destroy the mechanical, optical, and laser properties which will restrict the use of the crystals. Generally, the chemical etching method is an important and direct technique to investigate the defect structure of a single crystal. As we all know, acid and alkali are often used as the etchant to dissolve the dislocation sites.

The crystal of Tm,Ho:GdYTaO₄ and Nd:GdYNbO₄ are etched with KOH. Their dislocation etching pit patterns on the (100), (010), and (001) crystallographic faces are shown in Figures 2 and 3. Figure 2a,c exhibit the similar triangular prism, different from Figure 2b: rhombohedral. Similarly, the shape of the etching pits of Nd:GdYNbO₄ on (100) and (001) crystallographic faces are both present in strip shape, but not completely equivalent, as shown in Figure 3. Dislocations are typical defects introduced by the lattice distortion due to the incorporation of impurities and usually found in the molecules or atoms with the weak chemical bond. In the process of chemical etching, the weakest and unstable bonds are broken and form the specific etching pits. Therefore, dislocation etching pits have close relations with the atomic arrangement and symmetry.

**Figure 2.** Dislocation etching pit patterns of Tm,Ho:GdYTaO₄ crystal at three different crystalline faces: (a) (100); (b) (010); and (c) (001).**Figure 3.** Dislocation etching pit patterns of Nd:GdYNbO₄ crystal at three different crystalline faces: (a) (100); (b) (010); and (c) (001).

2.4. Measurements

All the absorption spectra were recorded by a VIS-NIR-IR spectrophotometer PE lambda 950 (PerkinElmer, Waltham, MA, USA). The excitation and emission spectra were measured by a fluorescence spectrometer FLSP920 (Edinburgh, UK), with an excitation source of Xenon lamp or diode laser. An Opolette 355I (Carlsbad, CA, USA) was used to measure the fluorescence decay curves. Thermal expansion behavior of crystals along a , b , and c axes were measured in the temperature range of 300–893 K using a thermal dilatometer DIL-402C (Netzsch, Selbe, Germany) with a heating rate of 5 K/min. The samples coated with graphite were used for the measurements of specific heat and thermal diffusivity along the a , b , and c axes by a laser flash apparatus LFA457 (Netzsch, Selbe, Germany)

2.5. Judd–Ofelt Calculation

The Judd–Ofelt (J–O) theory [18,19] has been successfully applied to various systems doped with rare-earth ions. The great advantage of the J–O theory is the ability to express the probability of any transition between two f^n states with only three intensity parameters (Ω_2 , Ω_4 , Ω_6) which can be obtained from absorption spectra. Moreover, spectral parameters, such as line strength (S), oscillator strength (f), transition probability (A), and radiative lifetime (τ), can be calculated with absorption spectrum. The experimental oscillator strength from the initial state $|SLJ\rangle$ to the final state $|S'L'J'\rangle$ was calculated as follows:

$$f = \frac{4m\epsilon_0c^2}{Ne^2\bar{\lambda}^2} \int \alpha(\lambda)d\lambda \quad (1)$$

where $\alpha(\lambda)$ is absorption coefficient, N is the total number of active ions per unit volume, m is the mass of the electron, ϵ_0 is permittivity of vacuum, c is the velocity of light in vacuum, e is the electron charge, and λ is given as Equation (2):

$$\bar{\lambda} = \frac{\int \lambda\alpha(\lambda)d\lambda}{\int \alpha(\lambda)d\lambda} \quad (2)$$

However, under certain simplifying assumptions, the oscillator strength (f) can be expressed as the sum of electric-dipole (f_{ed}) and magnetic-dipole (f_{md}) oscillator strength:

$$f = f_{ed} + f_{md} \quad (3)$$

Additionally, the relationships of oscillator strength and line strength are shown as follow:

$$S_{ed}(SLJ \rightarrow S'L'J') = \frac{9n}{(n^2 + 2)^2} \frac{3h(2J + 1)\bar{\lambda}}{8\pi^2mc} f_{ed} \quad (4)$$

$$S_{md}(SLJ \rightarrow S'L'J') = \frac{3h(2J + 1)\bar{\lambda}}{8\pi^2mcn} f_{md} \quad (5)$$

where J is the total angular momentum, n is the refractive index, and h is Planck constant. S_{ed} and S_{md} can be calculated easily with Equation (6):

$$S_{ed} = \sum_{t=2,4,6} \Omega_t |\langle SLJ || U^t || S'L'J' \rangle|^2 \quad (6)$$

$$S_{md} = \left(\frac{h}{4\pi mc}\right)^2 |\langle S'L'J' || L + 2S || SLJ \rangle|^2 \quad (7)$$

In the above formulas, $|\langle SLJ || U^t || S'L'J' \rangle|$ is the doubly reduced matrix elements of unitary tensor operator U^t with $t = 2, 4, 6$ between the state $|SLJ\rangle$ and $|S'L'J'\rangle$, $L + 2S$ is the magnetic dipole operator.

In addition, spontaneous transition probability (A), and radiative lifetime (τ) can be calculated with line strength:

$$A(SLJ \rightarrow S'L'J') = \left[\frac{16\pi^3 e^2}{3h\epsilon_0(J+1)\bar{\lambda}^3} \right] \times \left[\frac{n(n^2+2)^2}{9} S_{ed} + n^3 S_{md} \right] \quad (8)$$

$$\tau = \frac{1}{\sum_{J'} A(SLJ \rightarrow S'L'J')} \quad (9)$$

2.6. Emission Cross-Section Calculation

In this paper, all the emission cross-sections σ_{em} are calculated with the F–L formula:

$$\sigma_{em}(\lambda) = \frac{\lambda^5 \beta I(\lambda)}{8\pi n^2 c \tau \int \lambda I(\lambda) d\lambda} \quad (10)$$

where c is the speed of light, τ is the radiative lifetime of the upper energy level, n is the refractive index, and β is the branching ratio.

3. Scintillator Materials

3.1. GdTaO₄ and Nd:GdTaO₄ Crystals

In recent years there has been renewed interest in developing new scintillator materials characterized by high light yield, fast response, and high density [20–23]. Scintillators with high density and high atomic number are mostly desirable, because high stopping power can reduce the needed amount of scintillator materials and, thus, reduce the volume of the detector. GdTaO₄ is an attractive host and exhibits a high density (8.94 g/cm³). Attenuation length for GdTaO₄ is calculated to be 1 cm, only second to PWO (0.89 cm) [23,24]. Previously, GdTaO₄ crystal has been reported in a few papers [10,25,26], where the grown crystals are either with inclusions and twins [10] or with small size [26].

In our lab, nearly ten years have been spent on the Cz growth of GdTaO₄ single crystals. At first, an iridium wire is used to pull a crystal from the melt for obtaining the seed. With the seed, GdTaO₄ and Tb:GdTaO₄ bulk single crystals are successfully grown by the Cz method [27]. However, there are cracks, inclusions, and twins within these two crystals. After a long period of technological optimization, finally, a crack-free GdTaO₄ crystal with dimensions of $\Phi 23 \text{ mm} \times 30 \text{ mm}$ was grown successfully, which is the largest size so far [16].

The luminescence and scintillation properties of GdTaO₄ crystal have been studied in detail. Under the excitation of 273 nm, the GdTaO₄ crystal shows a strong emission band from 400 to 700 nm, with a highly asymmetrical shape [16]. To analyze the asymmetrical emission band further, a series of temperature-dependent luminescent spectra of GdTaO₄ crystal are measured. All of the emission spectra consist of two bands, 2.2 eV and 2.7 eV bands from 8 K to 300 K [28]. The emission intensity increases slightly as the temperature rising from 8 K to 80 K, and then decrease with increasing temperature. It is quenched rapidly above 150 K with the intensity decreasing by two orders of magnitude. The intensity variation of these two bands indicates the existence of thermal activation process. The activation energy of 2.2 eV and 2.7 eV bands is determined to be 156 meV and 175 meV, respectively. These two bands originate from different luminescent centers, which are tentatively assigned to self-trapped excitons (STE) localized at TaO₄³⁻ groups (2.7 eV) and to relaxed excitons related to lattice imperfections (2.2 eV) [28]. The photoluminescence decay shows two components, including a fast one of 30 ns with 53% and a relatively slow one of 452 ns with 47%. The scintillation decay consists of a fast component of 72.6 ns (9.5%) and a slow component of 1236.2 ns (90.5%). Meanwhile, the scintillation efficiency of GdTaO₄ is about four times as much as PWO by integrating

the area of the radioluminescence spectra. The relative light yield of GdTaO₄ is calibrated as 19 p.e./mes as that of PWO. Although, the scintillation decay of GTO is inferior to PWO, the latter presents a dominant decay of a dozen nanoseconds [24], the light yield of GdTaO₄ is higher than PWO.

In addition, the Nd:GdTaO₄ single crystal with density of 8.83 g/cm³ has been grown by Fang Peng et al. [29]. Its photoluminescence decay time of 417 nm from the 4*f*-4*f* transition of Nd³⁺ is 463 ns, and scintillation decay constants consist of 46.4 ns (48%) and 1199.7 ns (52%) under the excitation of 354 nm. The scintillation decay of Nd:GdTaO₄ is much faster than that of GdTaO₄, and the faster component percent is remarkably increased. This result may be caused by defects induced by Nd³⁺ doping. Moreover, because the concentration of Nd³⁺ is 0.67%, a rather low value, the light yield of Nd:GdTaO₄ can be estimated to be equal to that of GdTaO₄. However, the faster decay of Nd:GdTaO₄ is encouraging and makes it more effective in detecting high energy rays or particles than GdTaO₄.

3.2. LuTaO₄

Lutetium tantalate (LuTaO₄) is an efficient luminescent host material, especially excited by occurs by ionizing radiation [30,31]. LuTaO₄ also exhibits extremely high density (9.81 g/cm³), which is the highest among the present luminescent host materials. Therefore, LuTaO₄ may be an excellent heavy scintillator when it is doped with appropriate active ions, such as Nd³⁺. M'-type Lu_{1-x}Nd_xTaO₄ (*x*, 0.01–0.1) polycrystalline powders were synthesized by solid reaction method [32].

The emission at 418.5 nm corresponding to the ⁴D_{3/2}-⁴I_{13/2} transition of Nd³⁺ is strongest, and the fluorescence lifetime of 418.5 nm emission is measured to be approximately 263.2 ns, which is faster than that of BGO (300 ns) [32]. Meanwhile, LuTaO₄ can also emit directly. Therefore, LuTaO₄ can be expected as a very promising heavy substrate and heavy scintillator, which has potential applications in nuclear medicine and high energy detection. Thus, it is significant to explore the growth of LuTaO₄ and Nd:LuTaO₄ crystals.

Liu et al. [31] have spent long time on the LuTaO₄ crystal growth. However, unfortunately, it is hard to obtain single crystal. According to the XRD analysis, there are Lu₃TaO₇, M'-LuTaO₄, M-LuTaO₄ phases in the crystal pulled from LuTaO₄ melt, which indicates that the phase transition of the system Lu₂O₃-Ta₂O₅ is different from Gd₂O₃-Ta₂O₅. For designing or improving the single-crystal growth or ceramic preparation technique of LuTaO₄, Xing et al. [33] investigated the detailed phase relations of the Lu₂O₃-Ta₂O₅ system. The compounds containing 25–60 mol% Ta₂O₅ are prepared by solid-state reaction at sintering temperature from 1350 °C to 2058 °C. The sintered compound phases are studied by XRD in details. Cubic Lu₃TaO₇, M'-LuTaO₄, M-LuTaO₄, O-Ta₂O₅, and T-Ta₂O₅ are observed. With the temperature increases, there is an irreversible phase transition from M' to M-LuTaO₄ near 1770 °C in the composition of 30–52 mol% Ta₂O₅, and another phase transition from T-Ta₂O₅ to O-Ta₂O₅ at about 1685 °C when the ratio of Ta₂O₅ is >52 and ≤60 mol%. Finally, a phase diagram of the Lu₂O₃-Ta₂O₅ system in the range 0–100 mol% Ta₂O₅ is constructed, as shown in Figure 4. These results are helpful to explain the phase transition of Lu₂O₃-Ta₂O₅ system and to design the preparation technique of LuTaO₄ single crystals or ceramic scintillators.

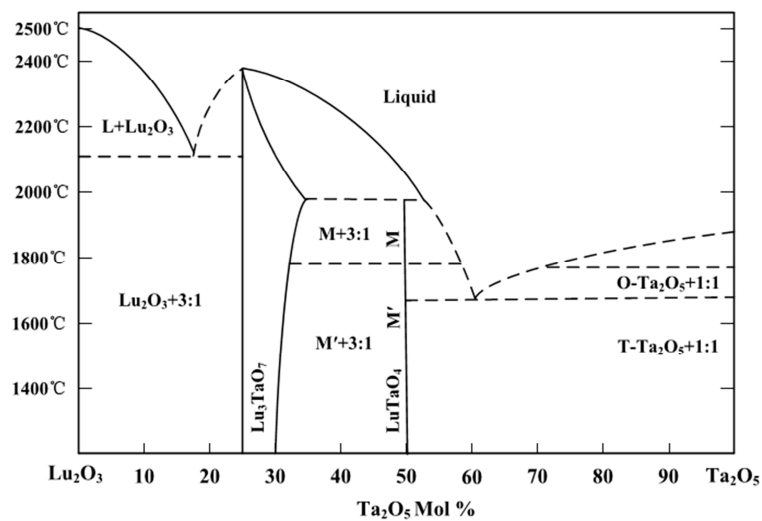


Figure 4. Phase-relation diagram of the Lu_2O_3 - Ta_2O_5 system [33]. Reproduced with permission from [Xue Xing et al., J. Am. Ceram. Soc.]; published by [John Wiley and Sons], [2015].

4. Laser Materials

In the following parts, we will briefly describe the spectral and laser properties of some active ion-doped orthotantalates and orthoniobates.

4.1. Er:GdTaO₄ Crystal

Trivalent erbium ion (Er^{3+}) has attracted wide attention due to its rich laser emission bands, such as, green laser (${}^2\text{H}_{11/2}, {}^4\text{S}_{3/2}$) \rightarrow ${}^4\text{I}_{15/2}$; red laser ${}^4\text{F}_{9/2} \rightarrow {}^4\text{I}_{15/2}$; 1.5–1.6 μm laser ${}^4\text{I}_{13/2} \rightarrow {}^4\text{I}_{15/2}$; 2.6–3 μm laser (${}^4\text{I}_{11/2} \rightarrow {}^4\text{I}_{13/2}$). These lasers can be applied in many different fields, including atmospheric monitoring, eye-safe laser, and medical treatment. Previously, 30 at% and 1 at% Er:GdTaO₄ crystals are grown by the Cz method [34,35]. According to the absorption spectra, the transition intensity parameters Ω_t ($t = 2, 4, 6$) are calculated by J–O theory and compared with other Er^{3+} -doped crystals, as shown in Table 2. Ω_2 is sensitive to the symmetry between the rare-earth ions and the ligand field. The spectroscopic quality factor Ω_4/Ω_6 of 1 at% Er:GdTaO₄ crystal is found to be 1.42, which is used to estimate the potential of active materials for laser operation when is linked to the luminescence branching ratios. The value of 1 at% Er:GdTaO₄ is comparable with those in other Er^{3+} -doped systems and larger than that of 30 at% Er:GdTaO₄ crystal. High Er^{3+} doping concentration is proposed to overcome the self-terminating “bottleneck” effect by inducing upconversion (UC) and cross-relaxation (CR) processes [36]. However, the fluorescence intensity of ${}^2\text{H}_{11/2}$, ${}^4\text{F}_{9/2}$, and ${}^4\text{S}_{3/2}$ states is quenched at high Er^{3+} concentration. The UC process depopulates the pumping level and the upper level of 1.6 μm laser and reabsorption in this wavelength increase with the increasing Er-concentration. Emission cross-section is an important parameters for evaluating the laser property of the materials, and larger cross-sections means easier laser realization. The largest emission cross-section of 30 at% Er:GdTaO₄ crystal is $0.655 \times 10^{-20} \text{ cm}^2$ at 2.631 μm , which indicates that 30 at% Er:GdTaO₄ crystal can be a promising laser medium around 2.6 μm [34]. The largest emission cross-section of 1 at% Er:GdTaO₄ crystal is $1.022 \times 10^{-20} \text{ cm}^2$ around 1.6 μm , which make it e great potential for near infrared laser generation. Furthermore, 1 at% Er:GdTaO₄ crystal also can be used as the green and red laser materials under some special environment such as at low temperature and this will be an important issue for our future research.

Table 2. Comparison of Ω_t values with other Er-doped hosts.

Crystals	$\Omega_2/10^{-20} \text{ cm}^2$	$\Omega_4/10^{-20} \text{ cm}^2$	$\Omega_6/10^{-20} \text{ cm}^2$	Ω_4/Ω_6
30 at% Er:YSGG [37]	0.23	0.86	0.37	2.32
0.6 at% Er:Gd ₂ SiO ₅ [38]	6.168	1.878	1.255	1.50
0.5 at% Er:Lu ₂ SiO ₅ [39]	4.451	1.614	1.158	1.39
30 at% Er:GdTaO ₄ [34]	0.98	1.17	4.67	0.25
1 at% Er:GdTaO ₄ [35]	7.553	1.999	1.404	1.42

4.2. Nd:GdTaO₄ and Nd:GdYTaO₄ Crystals

Nd:GdTaO₄ can be used not only as a heavy scintillator, but also as a new laser material. Nd:GdTaO₄ and Nd:Gd_{0.69}Y_{0.3}TaO₄ (Nd:GdYTaO₄) (1 at%) single crystals with high optical quality are grown successfully [40,41] and their luminescence and laser properties in near infrared wavelength are studied. The absorption cross-section of the Nd:GdTaO₄ crystal at 808 nm is $5.437 \times 10^{-20} \text{ cm}^2$, and the full width at half maximum (FWHM) of this absorption band is about 6 nm. The stimulated emission cross-section at 1066 nm is $3.9 \times 10^{-19} \text{ cm}^2$ and the measured lifetime of ⁴F_{3/2} level is 178.4 μs. A diode end-pumped Nd:GdTaO₄ laser at 1066 nm with the maximum output power of 2.5 W is achieved in the continuous-wave mode. The optical-to-optical conversion efficiency and slope efficiency are 34.6% and 36%, respectively. In addition, the fluorescence branching ratio of ⁴F_{3/2}→⁴I_{9/2} transition reaches 43%, indicating that Nd:GdTaO₄ may be an efficient laser medium at 920 nm.

The maximum absorption cross-section of Nd:GdYTaO₄ at 809 nm and the stimulated emission cross-section at 1066.6 nm are $6.886 \times 10^{-20} \text{ cm}^2$ and $22 \times 10^{-20} \text{ cm}^2$, respectively. The fluorescence lifetime is 182.4 μs. An 808 nm laser diode end-pumped continuous wave (CW) laser at 1066.5 nm is realized. The maximum output power of 2.37 W is obtained, corresponding to an optical conversion efficiency of 36.5% and a slope efficiency of 38%. Compared with the slope efficiency 36% of Nd:GdTaO₄, Nd:GdYTaO₄ shows an enhancement of the CW laser performance. Spectroscopic properties of Nd:GdTaO₄ and Nd:GdYTaO₄ are compared with other Nd-doped laser crystals, which are listed in Table 3. By comparison, Nd:GdYTaO₄ is a better novel laser crystal with low symmetry and has great potential in low to moderate level lasers.

Table 3. Comparison of spectroscopic properties of Nd:GdTaO₄ and Nd:GdYTaO₄ with other Nd-doped laser crystals [41].

Crystals	FWHM (@808 nm)	$\sigma_{\alpha} (10^{-20} \text{ cm}^2) (@808 \text{ nm})$	$\sigma_{em} (10^{-20} \text{ cm}^2) (@1.06 \mu\text{m})$	$\tau_{em} (\mu\text{s})$
Nd:GdYTaO ₄	6~12	6.9	22	182
Nd:GdTaO ₄	6	5.1	39	178
Nd:YAG	1.5	8.3	34	240
Nd:YVO ₄	4.4	40	156	99

4.3. Yb:GdTaO₄ Crystal

With only two multiplets ground state ²F_{7/2} and excited state ²F_{5/2}, the activator Yb³⁺ ion has attracted great attention, 1 at% and 5 at% Yb:GdTaO₄ are grown by our group. The main absorption peaks of 5 at% Yb:GdTaO₄ crystal locate at 930 nm, 956 nm, and 974 nm, and the corresponding absorption cross-sections are calculated to be $0.53 \times 10^{-20} \text{ cm}^2$, $0.84 \times 10^{-20} \text{ cm}^2$, and $0.65 \times 10^{-20} \text{ cm}^2$, respectively. However, 1 at% Yb:GdTaO₄ exhibited the bigger absorption cross-section, namely $0.81 \times 10^{-20} \text{ cm}^2$, $0.91 \times 10^{-20} \text{ cm}^2$, and $1.2 \times 10^{-20} \text{ cm}^2$ at 930 nm, 957 nm, and 974 nm, respectively. With the increase of Yb³⁺ ion concentration, the distance between Yb³⁺ ions becomes smaller, which causes the cross relaxation. Therefore, the absorption abilities of ground state ions are weaker. Oppositely, the emission cross-sections of 1 at% Yb:GdTaO₄ ($2.2 \times 10^{-20} \text{ cm}^2$ at 1016 nm; $1.36 \times 10^{-20} \text{ cm}^2$ at 1035 nm) are bigger than those of 5 at% Yb:GdTaO₄ ($0.54 \times 10^{-20} \text{ cm}^2$

at 1018 nm; 0.5×10^{-20} cm² at 1036 nm). According to the spectra results, 1 at% Yb:GdTaO₄ may be more suitable for laser putout.

4.4. Tm,Ho:GdYTaO₄ and Yb,Ho:GdYTaO₄ Crystal

The new wavelengths around 2.9 μm have attracted widely interests, due to their strong absorption in water, biological tissues, and vapor [42], which can be applied in medical, biological, and remote sensing. Moreover, laser wavelengths around 2.9 μm are also suitable pump sources for infrared optical parametric oscillation (OPO) or optical parametric generation (OPG) [43]. One possibility of generating 2.9 μm radiation is the ⁵I₆→⁵I₇ transition of Ho³⁺, which possesses rich energy levels [44]. Usually, Tm³⁺ are used to sensitize Ho³⁺ solid state lasers. Tm,Ho:GdYTaO₄ and Yb,Ho:GdYTaO₄ single crystals are grown and the spectral properties were studied in detail.

Their absorption spectra along *a*, *b*, and *c* axes are measured and the absorption coefficients are compared in Table 4. Their respective absorption coefficients along the *c* axis are larger than those along the other two directions. It indicates that the *c*-axis samples may be more beneficial for the laser performance by improving pumping efficiency.

Table 4. The absorption coefficient of *a*, *b*, and *c* directions at the pumping wavelength.

Crystals	α/cm^{-1} (³ H ₆ → ³ H ₄)			α/cm^{-1} (² F _{7/2} → ² F _{5/2})		
	<i>a</i>	<i>b</i>	<i>c</i>	<i>a</i>	<i>b</i>	<i>c</i>
Tm,Ho:GdYTaO ₄	2.75	2.79	3.88	–	–	–
Yb,Ho:GdYTaO ₄	–	–	–	5.08	5.60	9.67

The 2.9 μm emission spectra of Tm,Ho:GdYTaO₄ and Yb,Ho:GdYTaO₄ crystals are measured, excited by a 783 nm and 940 nm LD, respectively. Their emission cross-sections are calculated with F–L formula and compared in Figure 5. The main emission peaks of Tm,Ho:GdYTaO₄ are located at 2895, 2915 and 2932 nm. Similarly, strong peaks of Yb,Ho:GdYTaO₄ are located at 2865 and 2911 nm. The maximum emission cross-section of Tm,Ho:GdYTaO₄ at 2933 nm is 37.2×10^{-20} cm², which is larger than that of Yb,Ho:GdYTaO₄ (2911 nm, 17.6×10^{-20} cm²). It indicates that Tm,Ho:GdYTaO₄ may be easier to realize laser output than Yb,Ho:GdYTaO₄. In addition, the emission spectrum also indicates that the energy transfer between Yb³⁺–Ho³⁺ and Tm³⁺–Ho³⁺ ions can be realized successfully.

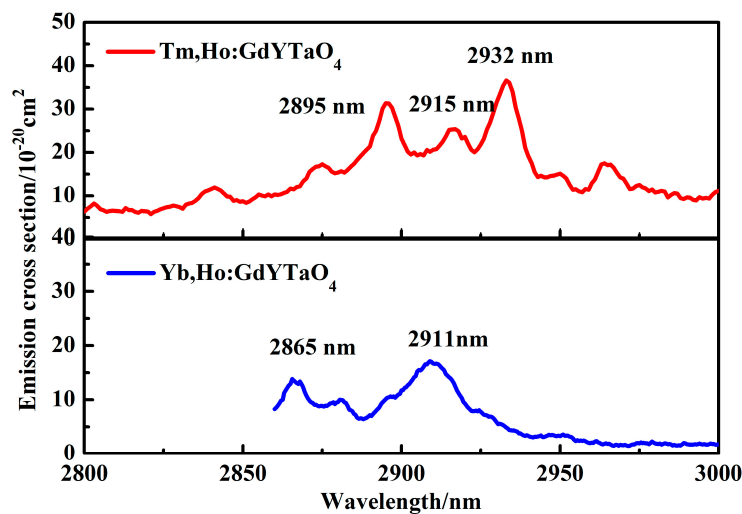


Figure 5. Emission cross-section spectra of Tm,Ho:GdYTaO₄ and Yb,Ho:GdYTaO₄ crystal at room temperature.

The fluorescence decay times are obtained. Their lifetimes of upper level and low level are shown in Table 5. Compared with other hosts, the Tm,Ho:GdYTaO₄ and Yb,Ho:GdYTaO₄ exhibit shorter lifetime of ⁵I₇ and longer lifetime of ⁵I₆, which are in favor of the population inversion and laser output. Moreover, the laser threshold of Yb,Ho:GdYTaO₄ may be lower than that of Tm,Ho:GdYTaO₄.

Table 5. Comparison of the lifetimes of ⁵I₇ and ⁵I₆ in different Ho³⁺-doped crystals [45–47].

Crystals	⁵ I ₆ /μs	⁵ I ₇ /ms	⁵ I ₇ / ⁵ I ₆
Tm,Ho:GdYTaO ₄	131	4.09	31.2
Yb,Ho:GdYTaO ₄	419	7.3	17.4
Yb,Ho:YSGG	585	10.2	17.4
Tm,Ho:LuAG	250	7.5	30.0
Tm,Ho:YAG	40	11.4	285

4.5. Yb:GdNbO₄ and Yb:YNbO₄

The intensive absorption broadband of 5 at% Yb:GdNbO₄ and 5 at% Yb:YNbO₄ between 900–1000 nm correspond to the typical transitions from ²F_{7/2} to the sublevels of ²F_{5/2} of Yb³⁺. There are three obvious absorption peaks of 5 at% Yb: GdNbO₄, located at 936, 955, and 975 nm, respectively. However, the absorption peaks of 5 at% Yb:YNbO₄ are 933, 955, and 974 nm. Their different locations probably are due to the small difference for the radius of Gd³⁺ (0.938 Å) and Y³⁺ (0.9 Å). Therefore, the environment of the crystal field around Yb³⁺ is a little different. The absorption cross-sections of 5 at% Yb:GdNbO₄ were calculated to 0.77 × 10⁻²⁰ cm², 0.85 × 10⁻²⁰ cm², 0.64 × 10⁻²⁰ cm², respectively. The absorption cross-section of 5 at% Yb:YNbO₄ were calculated to be 0.73 × 10⁻²⁰ cm², 1.85 × 10⁻²⁰ cm², 0.86 × 10⁻²⁰ cm², respectively.

Their refractive indices *n* were fitted with the following Sellmeier equation by the least square method:

$$n^2(\lambda, T) = A(T) + \frac{B(T)}{\lambda^2 - C(T)} + D(T)\lambda^2 \quad (11)$$

where *T* is crystal transmission. And the fitted results of 5 at% Yb:GdNbO₄ are *A* = 5.30671, *B* = 7711.03444 nm², *C* = 255,262.4962 nm², and *D* = -9.4997 × 10⁻⁸ (nm²)⁻¹. Similarly, *A* = 4.5440, *B* = 467,665.596 nm², *C* = -77,583.488 nm², and *D* = -6.352 × 10⁻⁸ (nm²)⁻¹ of 5 at% Yb:YNbO₄.

The emission cross-sections of Yb:GdNbO₄ and Yb:YNbO₄ crystal are calculated, and compared with other hosts, as shown in Table 6. The emission cross-sections of Yb:YNbO₄ are larger than that of Yb:GdNbO₄, and comparable to Yb:YAG. Therefore, it will be a promising near-infrared laser material.

Table 6. Absorption and emission cross-sections for Yb:YNbO₄, Yb:GdNbO₄, and some other Yb³⁺-doped crystals [48,49] at room temperature. (*σ_{abs}*: absorption cross-section; *σ_{em}*: emission cross-section).

Crystal	<i>σ_{abs}</i> /10 ⁻²⁰ cm ²	<i>σ_{em}</i> /10 ⁻²⁰ cm ²
Yb:YNbO ₄	0.73 (933 nm)	1.81 (1005 nm)
	1.85 (955 nm)	1.11 (1021 nm)
	0.86 (974 nm)	0.57 (1030 nm)
	0.44 (1003 nm)	
Yb:GdNbO ₄	0.87 (936 nm)	0.446 (1003)
	0.97 (955 nm)	0.487 (1018)
	0.85 (975 nm)	0.466 (1030)
	0.34 (1000 nm)	
Yb:Y ₂ O ₃	1.16 (978 nm)	0.95 (1032 nm)
Yb:YAG	0.86 (935 nm)	2.50 (1030 nm)
Yb:Lu ₂ O ₃	1.23 (978 nm)	0.95 (1034.5 nm)
Yb:GSO		0.66 (1030 nm)
	0.69 (925 nm)	0.38 (1048 nm)
		0.41 (1088 nm)
Yb:FAP	10.0 (905 nm)	5.9 (942 nm)

In addition, the preliminary laser experiment of Yb:GdNbO₄ is achieved. The pump source is an InGaAs LD with a maximum output powder of 25 W at around 976 nm in continuous mode. With a 3.54% transmission output coupler, the maximum laser power of 270 mW corresponding to the threshold of 6 W is obtained. The slope efficiency is 7.5%. High threshold pump power and low efficiency are mainly due to the crystal reabsorption, poor quality of the as-grown crystal, and crude plane-plane cavity. Good quality crystal and advanced cavity will improve the laser efficiency.

4.6. Nd:GdNbO₄, Nd:YNbO₄, Nd:GdYNbO₄, and Nd:GdLaNbO₄ Crystals

With the absorption spectra, the J–O intensity parameters $\Omega_{2,4,6}$, fluorescence branching ratios $\beta(J,J')$, radiative times τ_{rad} of Nd:GdNbO₄ (Nd:GNO), Nd:YNbO₄ (Nd:YNO), Nd:GdYNbO₄ (Nd:GYNO) and Nd:GdLaNbO₄ (Nd:GLNO) crystals are calculated by J–O theory [50–53]. The comparisons of $\beta(J,J')$ are listed in Table 7. As we can see, Nd:GLNO crystal has a relatively large value of $\beta_{11/2}$ than other Nd-doped niobate crystals, which indicates that this crystal may be more easily to generate lasers at around 1.06 μm . The comparisons of $\Omega_{2,4,6}$ are shown in Figure 6. The Ω_2 value of Nd:GLNO is higher than that of Nd:GNO crystal, point to the presence in Nd:GLNO crystal of Nd optical centers with lower environment symmetries determined by the doping of La³⁺ ions in GNO host, which induce a larger disorder around Nd³⁺ ions. Moreover, Nd:YNO crystal possesses the largest value of Ω_2 . The reason is that although these four crystals all belong to the monoclinic system, the angle of β in YNO is the largest, which indicates a lowest macroscopic symmetry in the Nd:YNO host. However, despite the Nd³⁺ ions possess a lowest environment symmetries in YNO host, which can supply a relatively strong crystal field for Nd³⁺ ions, the growth of Nd:YNO crystal is much harder than that of Nd:GNO crystal.

Table 7. Comparisons of τ_{rad} and $\beta(J,J')$ between Nd:GNO, Nd:YNO, Nd:GYNO, and Nd:GLNO crystals.

Crystals	$\beta_{9/2}$	$\beta_{11/2}$	$\beta_{13/2}$	$\beta_{15/2}$	τ_{rad}
1 at% Nd:GLNO	31.22	55.10	13.04	0.64	176
1 at% Nd:GYNO	33.04	53.88	12.47	0.61	156
2 at% Nd:GNO	31.53	54.90	12.95	0.62	178
1 at% Nd:YNO	34.39	52.98	12.05	0.58	152

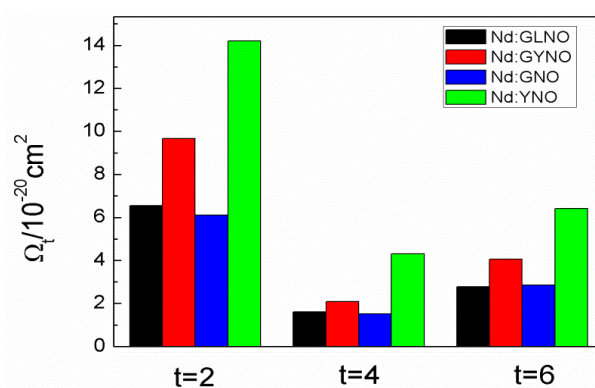


Figure 6. Comparison of $\Omega_{2,4,6}$ between Nd:GNO, Nd:YNO, Nd:GYNO, and Nd:GLNO crystals.

The room-temperature emission spectra of the as-grown Nd-doped niobate laser crystals at around 1.06 μm are shown in Figure 7. The strongest emission wavelength of Nd:GLNO, Nd:GNO, Nd:YNO, and Nd:GYNO are located at 1065.0 nm, 1065.7 nm, 1066 nm, and 1065.9 nm, respectively. Owing to the inhomogeneous broadening in the mixed crystal, Nd:GLNO and Nd:GYNO have a broader emission band at around 1.06 μm . In addition, stimulated emission cross-section can be estimated from the emission spectra using the F–L formula. Therefore, the stimulated emission cross-section values of

Nd:GLNO, Nd:GNO, Nd:YNO, and Nd:GYNO crystals at around 1.06 μm are estimated to be 18, 18.3, 22, and $20.5 \times 10^{-20} \text{ cm}^2$, respectively. Moreover, the fluorescence lifetimes of ${}^4\text{F}_{3/2} \rightarrow {}^4\text{I}_{11/2}$ transition are fitted to be 152, 178, 156, and 176.4 μs for Nd:YNO, Nd:GNO, Nd:GYNO, and Nd:GLNO, respectively. The small emission cross-section and long fluorescence lifetime indicates that the Nd:GLNO crystal possess good energy storage capacity, which is advantageous to its application in Q-switched laser.

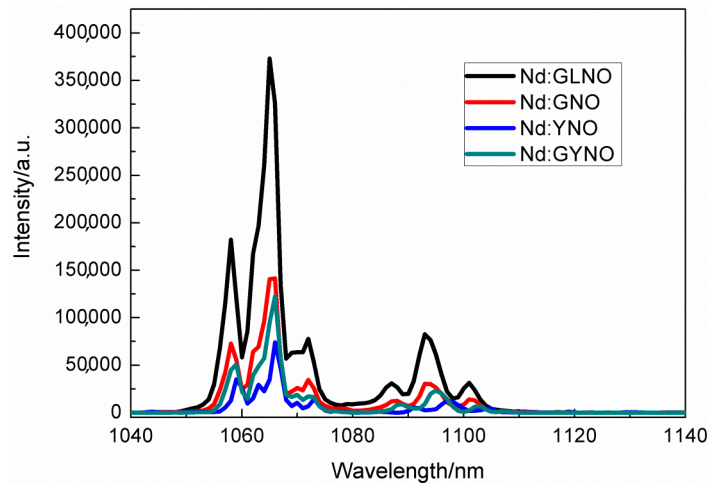


Figure 7. Emission spectra of Nd:GNO, Nd:YNO, Nd:GYNO, and Nd:GLNO crystals excited by 808 nm at room temperature.

In addition, laser performance of four crystals are operated based on a plano-plano resonator and the laser output power curves are shown in Figure 8. The transmission of output mirror in all of the laser experiment is 5.4% at 1.06 μm . The slope efficiency for Nd:YNO along *b*-orientation is 24.0%. The slope efficiency for Nd:GNO along three crystallographic axes (*a*-, *b*-, and *c*-) are 35.3%, 33.7%, and 28%, respectively. Additionally, the slope efficiency for Nd:GYNO along three crystallographic axes (*a*-, *b*- and *c*-) are 30.4%, 29.4% and 29.8%, respectively. Lastly, the slope efficiency for Nd:GLNO along *c*-orientation is 34.2%. Based on the above comparison of slope efficiency, Nd:GLNO is better than others.

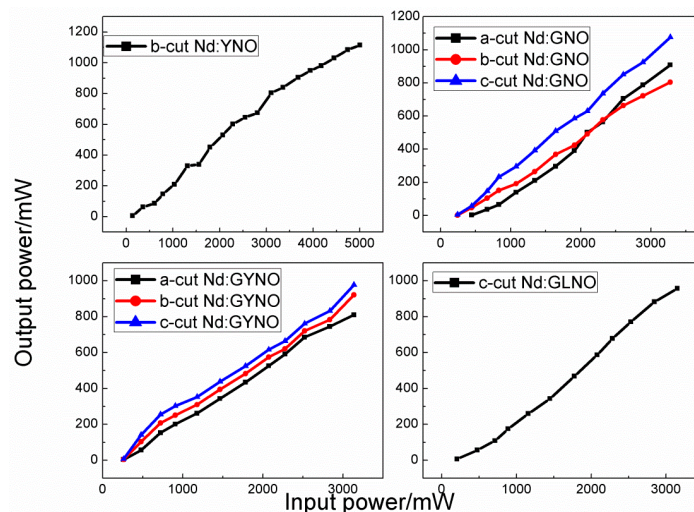


Figure 8. Laser output power of Nd:YNO, Nd:GNO, Nd:GYNO, and Nd:GLNO crystals versus incident power for different directions.

5. Crystal Field Calculation

5.1. Calculations of Energy Levels

Using the relativistic model of ab initio self-consistent $DV-X\alpha$ method [54,55] and effective Hamiltonian model [56], the crystal-field and spin-orbit parameters of Nd^{3+} in $GdTaO_4$ and $LuTaO_4$ have been calculated. The parameters of Nd^{3+} in $GdTaO_4$ and $LuTaO_4$ have been shown in Table 8.

Table 8. Parameters of Nd^{3+} in $GdTaO_4$ and $LuTaO_4$.

Parameters	Nd^{3+} : $GdTaO_4$	Nd^{3+} : $LuTaO_4$
B_0^2	−1891	778
B_2^2	−299	−321
B_0^4	702	−682
B_2^4	601 + 267i	−1017 + 795i
B_4^4	−302 + 149i	105 + 648i
B_0^6	−696	−421
B_2^6	248 + 620i	−302 − 118i
B_4^6	579 − 12i	−651 − 848i
B_6^6	77 − 168i	359 + 741i
ζ	998	902

The experimental energy level values of Nd^{3+} are obtained from the previous spectroscopic analysis. Then, the crystal-field and spin-orbit parameters from $DV-X\alpha$ method and effective Hamiltonian method and other free-ion parameters from Ref [57] were used as the initial values to fit the experimental energy levels of Nd^{3+} in $GdTaO_4$ and $LuTaO_4$ with the f -shell fitting program, which is developed by M. F. Ried with the Fortran language [58]. The calculated results, experimental results and the difference between the calculated values and experimental values are shown in Table 9.

Table 9. Energy levels of Nd^{3+} in rare earth tantalates.

$2s+1L_J$	Nd^{3+} Energy Levels of $GdTaO_4$			Nd^{3+} Energy Levels of $LuTaO_4$		
	E (calc)	E (exp)	ΔE (cm^{-1})	E (calc)	E (exp)	ΔE (cm^{-1})
$^4I_{9/2}$	−4.81	0	4.81	−21.81	0	21.81
	122.09	117	−5.09	105.21	115	9.79
	242.10	238	−4.10	162.71	151	−11.71
	372.17	367	−5.17	289.78	275	−14.78
$^4I_{11/2}$	489.45	498	8.55	640.44	631	−9.44
	2319.31	−	−	1978.34	1983	4.66
	2369.08	−	−	1992.01	2005	12.99
	2450.84	−	−	2058.63	2039	−19.63
	2516.72	−	−	2123.43	2123	−0.43
$^4I_{13/2}$	2592.42	−	−	2292.47	2304	11.53
	2656.79	−	−	2354.40	2361	6.60
	4619.13	4632	12.87	3924.45	3921	−3.45
	4672.95	4668	−4.95	3933.55	3939	5.45
	4735.59	4745	9.41	3991.05	3980	−11.05
	4829.13	4842	12.87	4055.60	4057	1.40
$^4I_{15/2}$	4873.80	−	−	4250.42	4260	9.58
	4936.67	4944	7.33	4297.58	4310	12.42
	5044.43	5036	−8.43	4383.78	4354	−29.78
	6874.39	6872	−2.39	5830.42	−	−
	7000.32	7013	12.68	5880.84	−	−
	7071.00	7084	13.00	5929.69	−	−
	7134.39	7148	13.61	5989.77	−	−
7226.49	7239	12.51	6349.72	−	−	
7322.92	7324	1.08	6405.49	−	−	
7462.48	7470	7.52	6552.21	−	−	
7621.33	−	−	6630.59	−	−	

Table 9. Cont.

$2s+1L_J$	Nd ³⁺ Energy Levels of GdTaO ₄			Nd ³⁺ Energy Levels of LuTaO ₄		
	E (calc)	E (exp)	ΔE (cm ⁻¹)	E (calc)	E (exp)	ΔE (cm ⁻¹)
$^4F_{3/2}$	11,617.98	11,615	-2.98	11,368.59	11,365	-3.59
	11,878.56	11,877	-1.56	11,451.70	11,450	-1.70
$^4F_{5/2} + ^2H_{9/2}(2)$	12,755.05	12,731	-24.05	12,336.64	12,341	4.36
	12,874.09	12,862	-12.09	12,390.72	12,409	18.28
	12,907.30	12,898	-9.30	12,510.25	12,509	-1.25
	12,954.06	12,935	-19.06	12,551.60	12,550	-1.60
	13,026.22	13,014	-12.22	12,599.59	12,590	-9.59
$^4F_{7/2} + ^4S_{3/2}$	13,185.56	13,171	-14.56	12,695.51	12,677	-18.51
	13,926.81	13,936	9.19	13,349.10	13,321	-28.10
	14,094.82	14,082	-12.82	13,400.94	13,382	-18.94
	14,151.69	14,163	11.31	13,487.04	13,497	9.96
	14,184.81	-	-	13,499.67	13,517	17.33
$^4F_{9/2}$				13,514.64	13,532	17.36
				13,611.03	13,623	11.97
	15,451.31	15,464	12.69	14,583.44	14,573	-10.44
	15,623.02	15,601	-22.02	14,795.59	14,767	-28.59
	15,675.85	15,664	-11.85	14,868.52	14,873	4.48
$^2H_{11/2}(2)$	15,740.08	-	-	15,842.02	15,844	1.98
	15,814.32	15,825	10.68	15,929.31	15,927	-2.31
	16,824.27	16,833	8.73	16,846.25	16,844	-2.25
	16,881.07	16,896	14.93	16,919.53	16,922	2.47
$^4G_{5/2} + ^2G_{7/2}$	16,911.49	-	-	17,058.50	17,036	-22.50
	16,947.09	16,965	17.91	17,168.31	17,194	25.69
	17,629.64	17,646	16.36	17,214.23	17,221	6.77
	17,898.56	17,884	-14.56	17,236.09	17,256	19.91
$^4G_{7/2}$	17,959.88	17,940	-19.88	17,261.02	-	-
				17,288.86	-	-
				17,455.47	17,459	3.53
	19,681.74	19,697	15.26	18,707.70	18,711	3.30
$^2K_{13/2} + ^4G_{9/2}$	19,834.97	19,825	-9.97	18,811.84	18,811	-0.84
				18,914.48	18,924	9.52
				18,949.08	-	-
	20,511.95	20,502	-9.95	19,135.78	19,150	14.22
$^2G_{9/2}(1) + ^4G_{11/2} + ^2D_{3/2}(1) + ^2K_{15/2}$	20,680.22	20,687	6.78	19,292.55	19,307	14.45
				19,378.41	19,379	0.59
	21,672.12	21,678	5.88	20,780.79	20,790	9.21
	22,014.24	-	-	20,844.56	20,843	-1.56
	22,240.88	22,230	-10.88	20,977.02	20,973	-4.02
	22,847.41	22,841	-6.41	21,022.94	21,017	-5.94
				21,098.53	21,088	-10.53
				21,183.83	21,194	10.17
				21,519.96	21,523	3.04
$^2P_{1/2}$				21,604.87	21,606	1.13
				21,762.06	21,774	11.94
$^2D(1)_{5/2}$	23,973.77	23,960	-13.77	23,085.11	23,095	9.89
				23,597.10	23,585	-12.10
				23,698.37	23,685	-13.37
$^2P_{3/2}$				23,811.15	23,787	-24.15
				25,952.60	25,965	12.40
$^4D_{3/2}$				26,074.57	26,074	-0.57
	27,638.97	27,628	-10.97	27,535.98	27,539	3.02
			27,648.17	27,636	-12.17	

Table 9. Cont.

$2s+1L_J$	Nd ³⁺ Energy Levels of GdTaO ₄			Nd ³⁺ Energy Levels of LuTaO ₄		
	E (calc)	E (exp)	ΔE (cm ⁻¹)	E (calc)	E (exp)	ΔE (cm ⁻¹)
⁴ D _{5/2}				27,840.16 28,029.62	27,848 28,027	7.84 -2.62
² I _{11/2} + ⁴ D _{1/2}	29,682.98	29,676	-6.98	28,221.24 28,328.95	28,218 28,324	-3.24 -4.95
² I _{13/2} + ² L _{17/2}	31,640.01 ...	31,650 -	9.99 -	28,928.96 29,682.43	28,917 29,677	-11.96 -5.43
⁴ D _{7/2} + ² D(2) _{3/2}				30,182.43 32,893.13	30,177 32,895	-5.43 1.87
² H(1) _{11/2}				33,790.34	33,806	15.66
² F(2) _{5/2}	35,808.85 ...	35,822 -	13.15 -	34,382.58 ...	- -	- -

From Table 8, most of the calculated levels are quite consistent with experimental energy levels. In Nd³⁺:LuTaO₄, among the 152 experimental energy levels, there are four Stark levels (4354, 13,321, 14,767, and 17,194 cm⁻¹) with poor fitting quality with deviations of -29.78, -28.10, -28.59, and 25.69 cm⁻¹, respectively. Additionally, in Nd³⁺:GdTaO₄, there are only two Stark levels (12,731 and 15,601 cm⁻¹) with poor fitting quality with deviations of -24.05 and -22.02 cm⁻¹, respectively. The deviation of calculated energy levels and experimental energy levels are less than 30 cm⁻¹, which indicates that the fitted energy levels results are satisfactory.

It was concluded that the *J*-mixing effect does not play any significant role in the low-lying energy levels from the fitting results, especially for ⁴I_{9/2}, ⁴I_{11/2}, ⁴I_{13/2}, ⁴I_{15/2}, and ⁴F_{3/2} multiplets. However, at the higher-energy side, the *J*-mixing effect is clearly appreciable because the Stark components are overlapping with adjacent multiplets. On the other hand, the *M*-mixing effect is very clear for all energy levels.

5.2. Crystal Field Analysis

The experimental energy levels of Nd³⁺ give a basic set for a reliable energy level simulation. A model with 30 parameters including 16 free-ion and 14 crystal-field parameters is used for Nd³⁺ in rare earth tantalates, with the root mean square deviation (σ) of 12.66 and 14.6 cm⁻¹. In the simulation process, it could be stated that the relative positions of some experimental energy levels depend on α , β , γ , and T^i . Such as the energy levels of ⁴S_{3/2} and ⁴F_{7/2}, ⁴G_{9/2} and ²K_{13/2}, ⁴G_{11/2}, and ²K_{15/2} [59].

The free-ions and crystal-field parameters of Nd³⁺ in GdTaO₄, LuTaO₄, and YAlO₃ hosts are shown in Table 10.

Table 10. Comparing the free-ions and crystal-field parameters.

Parameters	Nd ³⁺ :GdTaO ₄	Nd ³⁺ :LuTaO ₄	Nd ³⁺ : YAlO ₃ [60]
E_{avg}	25,167	24,141	24,119
F^2	73,018	73,290	70,925
F^4	52,789	60,030	50,794
F^6	35,757	44,220	35,424
ζ	1034	883	875
α	21.34	11.22	23
β	-593	-436	-691
γ	1445	-1694	1690
T^2	[298]	[298]	[458]
T^3	[35]	[35]	[38]
T^4	[59]	[59]	[75]
T^6	[-285]	[-285]	[-290]
T^7	[332]	[332]	[237]
T^8	[305]	[305]	[496]

Table 10. Cont.

Parameters	Nd ³⁺ :GdTaO ₄	Nd ³⁺ :LuTaO ₄	Nd ³⁺ : YAlO ₃ [60]
<i>M</i>	2.11	2.11	1.90
<i>P</i>	192	192	206
<i>B</i> ₀ ²	−1560	591	−154
<i>B</i> ₂ ²	−415	−153 − 70i	578
<i>B</i> ₀ ⁴	626	−753	−541
<i>B</i> ₂ ⁴	422+315i	−1428 + 611i	967 + 24i
<i>B</i> ₄ ⁴	244 + 18i	516 + 898i	−309+608i
<i>B</i> ₀ ⁶	−613	−522	−671
<i>B</i> ₂ ⁶	−301 + 807i	−147 − 43i	512 − 18i
<i>B</i> ₄ ⁶	−100 − 103i	172 − 820i	1611 + 0i
<i>B</i> ₆ ⁶	−279 − 107i	533 + 864i	0 + 132i
<i>σ</i>	12.66	14.6	15.50
<i>N_v</i>	2959	2927	2545

The values of free-ions parameters of Nd³⁺ in rare earth tantalates are similar to those in YAlO₃ hosts. However, the electrostatic interaction between two 4*f* electrons of Nd³⁺ doped in rare earth tantalates is stronger than that of Nd³⁺ in YAlO₃, because of the more delocalized electrons and decreased Slater integrals. With the Slater integrals decreasing, the individual ^{2S+1}L_J state will be lowered, so the energy positions of ²P_{1/2} are 23,960 and 23,164 cm^{−1} for Nd³⁺ in GdTaO₄ and YAlO₃ hosts, respectively. The spin-orbit interaction varies slightly for these two hosts whereas the other free-ion parameters show no clear trend. This is because Nd³⁺ ion occupies the 4*e* sites of Gd(Lu) with C₂ point symmetry, and each of the ions in rare earth tantalates is octahedrally coordinated with six O forming a distorted square antiprism, whereas Nd³⁺ ion occupies the 4*c* sites of Y with C₅ point symmetry, and each of the ions is dodecahedrally coordinated to eight O in YAlO₃.

The values of crystal-field parameters are affected by the distances, bonding angles, and the nature of ligands. The crystal-field parameters *B*⁶ are only related to the ions of the nearest neighbor rather than the ions of next nearest neighbor and further, while *B*² and *B*⁴ are not only related to the ions of the nearest neighbor but also the ions of next nearest neighbor and further. In Table 8, *B*² and *B*⁴ of Nd³⁺ ions have relatively large differences among these rare earth tantalates and YAlO₃, but the crystal-field parameters *B*⁶ are close to each other. This is because the interaction between 4*f* electrons of Nd³⁺ and Ta⁵⁺, Gd³⁺, and Lu³⁺ surrounding Nd³⁺ are strong in rare earth tantalates. It indicates that the charge interpenetration and coulomb exchange of Nd³⁺ in rare earth tantalates are stronger than those of Nd³⁺ in YAlO₃ while covalency and overlap of Nd³⁺ in rare earth tantalates are weaker than those of Nd³⁺ in YAlO₃. In fact, the overlap and coulomb exchange are responsible for about half the total parameters values, and the other half comes mostly from covalency. When the charge penetration contributions are taken into account, the magnitudes of the net electrostatic contributions are only of the order of 10% of the combined contributions from covalency and exclusion. Thus, in the analysis of the lanthanide crystal fields, approximations which neglect electrostatic contributions are likely to be far more realistic than those which neglect overlap and covalency contributions.

The *N_v* values are calculated from the two sets of crystal-field parameters, which are defined in terms of the length rather than the rotational invariants of the crystal-field parameters vector in the spherical harmonics space, allowing a direct comparison of the crystal-field strength in any type of symmetry[59]. From Table 9, we see that the contribution of rank six crystal-field parameters to the total crystal-field strength is larger in rare earth tantalates than that in YAlO₃. Taking into consideration the electronegativity values of Gd(Lu) and Y ions, it might be concluded that in rare earth tantalates crystals, the neighbor ions of impurities are slightly nearer than those in the YAlO₃ crystals. Thus, the contribution to the total crystal field of these neighbors is greater in rare earth tantalates than that in the YAlO₃ hosts, as it was calculated. The *N_v* of Nd³⁺ in rare earth tantalates is larger than that in YAlO₃, therefore, crystal-field interaction of rare earth tantalates is stronger than that of YAlO₃.

6. Conclusions

- i. Rare-earth orthotantalates have high density deserve to be studied as scintillators. Large volume and high-quality single crystals are grown and their properties are researched systematically by our group. The scintillation decay time of Nd:GdTaO₄ single crystal is faster than GdTaO₄ single crystal. LuTaO₄ has the highest density 9.8 g/cm³ among the present luminescent material hosts, and the fluorescence lifetime of Nd:LuTaO₄ is about 263.2 ns and expected as the most promising heavy scintillator.
- ii. Er:GdTaO₄ and Tm,Ho:GdYTaO₄ single crystals have good visible and mid-infrared fluorescence properties and can be the potential laser materials. Nd³⁺, Yb³⁺-doped orthotantalates and orthoniobates have been realized laser output, which prove that they can be used as laser matrix hosts successfully.
- iii. The ab initio self-consistent DV-X α method has been used in its relativistic model to investigate the crystal-field and spin-orbit parameters of Nd³⁺ doped in rare earth tantalates. The deviations of the calculated energy levels and experimental energy levels are less than 30 cm⁻¹, which indicates that the energy levels fitting results are satisfactory. Through the calculation of the crystal field parameters it is shown that the crystal field is strong and is beneficial to the widen of the ion absorption band, which indicated that rare-earth orthotantalates will be promising laser crystal materials.

Acknowledgments: This work was financially supported by the National Natural Science Foundation of China (Grants Nos. 51502292, 51702322, and 61405206), National Key Research and Development Program of China (Grant No. 2016YFB0402101).

Author Contributions: Thank all the co-authors' contributions for this paper. Renqin Dou researched the Yb-doped niobates and Tm/Yb,Ho-doped tantalates and wrote the paper; Yuanzhi Chen studied the Er-doped tantalates; Shoujun Ding analyzed the Nd-doped niobates; Fang Peng performed the Nd-doped tantalates; Wenpeng Liu contributed crystal growth; Dunlu Sun revised the paper.

Conflicts of Interest: The authors declare no conflict of interest.

References

1. Abe, R.; Higashi, M.; Sayama, K.; Abe, Y.; Sugihara, H. Photocatalytic activity of R₃MO₇ and R₂Ti₂O₇ (R = Y, Gd, La; M = Nb, Ta) for water splitting into H² and O². *J. Phys. Chem. B* **2006**, *110*, 2219–2226. [[CrossRef](#)] [[PubMed](#)]
2. Haugsrud, R.; Norby, T. Proton conduction in rare-earth ortho-niobates and ortho-tantalates. *Nat. Mater.* **2006**, *5*, 193–196. [[CrossRef](#)]
3. Zhang, H.; Wang, Y.; Xie, L. Luminescent properties of Tb³⁺ activated GdTaO₄ with M and M' type structure under UV-VUV excitation. *J. Lumin.* **2010**, *130*, 2089–2092. [[CrossRef](#)]
4. Forbes, T.Z.; Nyman, M.; Rodriguez, M.A.; Navrotsky, A. The energetics of lanthanum tantalate materials. *J. Solid State Chem.* **2010**, *183*, 2516–2521. [[CrossRef](#)]
5. Sych, A.M.; Golub, A.M. Niobates and Tantalates of Trivalent Elements. *Uspekhi Khimii* **1977**, *46*, 417–444.
6. Gundobin, N.V.; Petrov, K.I.; Plotkin, S.S. Vibration-Spectra and Structure Ln₃MO₇-Type Niobates and Tantalates. *Zhurnal Neorganicheskoi Khimii* **1977**, *22*, 2973–2977.
7. Siqueira, K.P.F.; Carmo, A.P.; Bell, M.J.V.; Dias, A. Optical properties of undoped NdTaO₄, ErTaO₄ and YbTaO₄ ceramics. *J. Lumin.* **2016**, *179*, 146–153. [[CrossRef](#)]
8. Blasse, G.; Brill, A. Luminescence phenomena in compounds with fergusonite structure. *J. Lumin.* **1970**, *3*, 109–131. [[CrossRef](#)]
9. Voloshyna, O.; Neicheva, S.V.; Starzhinskiy, N.G.; Zenyaa, I.M.; Gridina, S.S.; Baumerb, V.N.; Sidletskiya, O.T. Luminescent and scintillation properties of orthotantalates with common formulae RETaO₄ (RE = Y, Sc, La, Lu and Gd). *Mater. Sci. Eng. B* **2013**, *178*, 1491–1496. [[CrossRef](#)]
10. Kazakova, L.I.; Bykov, I.S.; Dubovsky, A.B. The luminescence of rare-earth tantalate single crystals. *J. Lumin.* **1997**, *72–74*, 211–212. [[CrossRef](#)]

11. Brixner, L. On the structural and luminescent properties of the M' LnTaO_4 rare earth tantalates. *J. Electrochem. Soc.* **1983**, *130*, 2435–2443. [[CrossRef](#)]
12. Stubičan, V. High-Temperature Transitions in Rare-Earth Niobates and Tantalates. *J. Am. Ceram. Soc.* **1964**, *47*, 55–58. [[CrossRef](#)]
13. Siqueira, K.P.F.; Carvalho, G.B.; Dias, A. Influence of the processing conditions and chemical environment on the crystal structures and phonon modes of lanthanide orthotantalates. *Dalton Trans.* **2011**, *40*, 9454–9460. [[CrossRef](#)] [[PubMed](#)]
14. Liu, B.; Han, K.; Liu, X.; Gu, M.; Huang, S.; Ni, C.; Qi, Z.; Zhang, G. Luminescent properties of GdTaO_4 and $\text{GdTaO}_4:\text{Eu}^{3+}$ under VUV-UV excitation. *Solid State Commun.* **2007**, *144*, 484–487. [[CrossRef](#)]
15. Liu, X.; Chen, S.; Gu, M.; Wu, M.; Qiu, Z.; Liu, B.; Ni, C.; Huang, S. A novel M' -type $\text{LuTaO}_4:\text{Ln}^{3+}$ ($\text{Ln} = \text{Eu}, \text{Tb}$) transparent scintillator films. *Opt. Mater. Express* **2014**, *4*, 172–178. [[CrossRef](#)]
16. Yang, H.; Peng, F.; Zhang, Q.; Guo, C.; Shi, C.; Liu, W.; Sun, G.; Zhao, Y.; Zhang, D.; Sun, D.; et al. A promising high-density scintillator of GdTaO_4 single crystal. *CrystEngComm* **2014**, *16*, 2480–2485. [[CrossRef](#)]
17. Ning, K.; Zhang, Q.; Zhang, D.; Fan, J.; Sun, D.; Wang, X.; Hang, Y. Crystal growth, characterization of NdTaO_4 : A new promising stoichiometric neodymium laser material. *J. Cryst. Growth* **2014**, *388*, 83–86. [[CrossRef](#)]
18. Ofelt, G.S. Intensities of Crystal Spectra of Rare-Earth Ions. *J. Chem. Phys.* **1962**, *37*, 511–520. [[CrossRef](#)]
19. Judd, B.R. Optical Absorption Intensities of Rare-Earth Ions. *Phys. Rev.* **1962**, *127*, 750–761. [[CrossRef](#)]
20. Nikl, M.; Bruza, P.; Panek, D.; Vrbova, M.; Mihokova, E.; Mares, J.A.; Beitlerova, A.; Kawaguchi, N.; Fukuda, K.; Yoshikawa, A. Scintillation characteristics of LiCaAlF_6 -based single crystals under X-ray excitation. *Appl. Phys. Lett.* **2013**, *102*, 161907. [[CrossRef](#)]
21. Rooh, G.; Kim H, J.; Park, H.; Kim, S. Investigation of scintillation and luminescence properties of cerium doped $\text{Rb}_2\text{LiGdCl}_6$ single crystals. *J. Cryst. Growth* **2013**, *377*, 28–31. [[CrossRef](#)]
22. Nikl, M.; Solovieva, N.; Pejchal, J.; Shim, J.B.; Yoshikawa, A.; Fukuda, T.; Vedda, A.; Martini, M.; Yoon, D.H. Very fast $\text{Yb}_x\text{Y}_{1-x}\text{AlO}_3$ single-crystal scintillators. *Appl. Phys. Lett.* **2004**, *84*, 882–884. [[CrossRef](#)]
23. Moses, W.W.; Weber, M.J.; Derenzo, S.E.; Perry, D.; Berdahl, P.; Boatner, L.A. Prospects for dense, infrared emitting scintillators. *IEEE Trans. Nucl. Sci.* **1998**, *45*, 462–466. [[CrossRef](#)]
24. Lecoq, P.; Dafinei, I.; Auffray, E.; Schneegans, M.; Korzhik, M.V.; Missevitch, O.V.; Pavlenko, V.B.; Fedorov, A.A.; Annenkov, A.N.; Kostylev, V.L.; et al. Lead tungstate (PbWO_4) scintillators for LHC EM calorimetry. *Nucl. Instrum. Methods Phys. Res. Sect. A* **1995**, *365*, 291–298. [[CrossRef](#)]
25. Almeida Silva, R.; Tirao, G.; Cusatis, C.; Andreetta, J.P. Growth and X-ray characterization of $\text{Gd}_x\text{Yb}_{1-x}\text{TaO}_4$ ($0 \leq x \leq 1$) single crystals with large lattice spacing gradient. *J. Cryst. Growth* **2005**, *277*, 308–313. [[CrossRef](#)]
26. Almeida Silva, R.; Tirao, G.; Cusatis, C.; Andreetta, J.P. Growth and structural characterization of M-type GdTaO_4 single crystal fiber. *J. Cryst. Growth* **2005**, *274*, 512–517. [[CrossRef](#)]
27. Liu, W.; Zhang, Q.; Zhou, W.; Gu, C.; Yin, S. Growth and Luminescence of M-Type GdTaO_4 and Tb: GdTaO_4 Scintillation Single Crystals. *IEEE Trans. Nucl. Sci.* **2010**, *57*, 1287–1290. [[CrossRef](#)]
28. Yang, H.; Peng, F.; Zhang, Q.; Shi, C.; Guo, C.; Wei, X.; Sun, D.; Wang, X.; Dou, R.; Xing, X.; et al. Temperature-dependent luminescence of GdTaO_4 single crystal. *J. Lumin.* **2015**, *160*, 90–94. [[CrossRef](#)]
29. Peng, F.; Liu, W.; Zhang, Q.; Yang, H.; Shi, C.; Mao, R.; Sun, D.; Luo, J.; Sun, G. Crystal growth, optical and scintillation properties of Nd^{3+} doped GdTaO_4 single crystal. *J. Cryst. Growth* **2014**, *406*, 31–35. [[CrossRef](#)]
30. Blasse, G.; Dirksen, G.J.; Brixner, L.H.; Crawford, M.K. Luminescence of Materials Based On LuTaO_4 . *J. Alloy. Compd.* **1994**, *209*, 1–6. [[CrossRef](#)]
31. Liu, W.; Zhang, Q.; Ding, L.; Sun, D.; Luo, J.; Yin, S. Photoluminescence properties of $\text{LuTaO}_4:\text{RE}^{3+}$ ($\text{RE}^{3+} = \text{Eu}^{3+}, \text{Tb}^{3+}$) with M' -type structure. *J. Alloy. Compd.* **2009**, *474*, 226–228. [[CrossRef](#)]
32. Zhao, Y.; Zhang, Q.; Guo, C.; Shi, C.; Peng, F.; Yang, H.; Sun, D.; Luo, J.; Liu, W. The luminescence properties of the high-density phosphor $\text{Lu}_{1-x}\text{Nd}_x\text{TaO}_4$. *J. Lumin.* **2014**, *155*, 165–169. [[CrossRef](#)]
33. Xing, X.; Wang, X.; Zhang, Q.; Sun, G.; Shi, C.; Liu, W.; Sun, D.; Yin, S. High-Temperature Phase Relations in the $\text{Lu}_2\text{O}_3\text{-Ta}_2\text{O}_5$ System. *J. Am. Ceram. Soc.* **2016**, *99*, 1042–1046. [[CrossRef](#)]
34. Yang, H.; Zhang, Q.; Zhou, P.; Ning, K.; Gao, J.; He, Y.; Luo, J.; Sun, D.; Yin, S. Czochralski growth and optical investigations of $\text{Er}^{3+}:\text{GdTaO}_4$ laser crystal. In Proceedings of the SPIE 8206, Pacific Rim Laser Damage 2011: Optical Materials for High Power Lasers, Shanghai, China, 12 January 2012.

35. Chen, Y.; Peng, F.; Zhang, Q.; Liu, W.; Dou, R.; Ding, S.; Luo, J.; Sun, D.; Sun, G.; Wang, X. Growth, structure and spectroscopic properties of 1 at.% Er³⁺: GdTaO₄ laser crystal. *J. Lumin.* **2017**, *192*, 555–561. [[CrossRef](#)]
36. Lupei, V.; Georgescu, S.; Florea, V. On the dynamics of population inversion for 3 μm Er³⁺ lasers. *IEEE J. Quantum Electron.* **1993**, *29*, 426–434. [[CrossRef](#)]
37. Su, J.; Yang, C.; Li, Q.; Zhang, Q.; Luo, J. Optical spectroscopy of Er:YSGG laser crystal. *J. Lumin.* **2010**, *130*, 1546–1550. [[CrossRef](#)]
38. Xu, X.; Zhao, G.; Wu, F.; Xu, W.; Zong, Y.; Wang, X.; Zhao, Z.; Zhou, G.; Xu, J. Growth and spectral properties of Er:Gd₂SiO₅ crystal. *J. Cryst. Growth* **2008**, *310*, 156–159. [[CrossRef](#)]
39. Ding, Y.; Zhao, G.; Xu, X. Crystal growth and spectroscopic properties of erbium doped Lu₂SiO₅. *J. Cryst. Growth* **2010**, *312*, 2103–2106. [[CrossRef](#)]
40. Peng, F.; Yang, H.; Zhang, Q.; Luo, J.; Liu, W.; Sun, D.; Dou, R.; Sun, G. Spectroscopic properties and laser performance at 1066 nm of a new laser crystal Nd:GdTaO₄. *Appl. Phys. B* **2015**, *118*, 549–554. [[CrossRef](#)]
41. Peng, F.; Yang, H.; Zhang, Q.; Luo, J.; Sun, D.; Liu, W.; Sun, G.; Dou, R.; Wang, X.; Xing, X. Growth, thermal properties, and LD-pumped 1066 nm laser performance of Nd³⁺ doped Gd/YTaO₄ mixed single crystal. *Opt. Mater. Express* **2015**, *5*, 2536–2544. [[CrossRef](#)]
42. Tempus, M.; Luthy, W.; Weber, H.P.; Ostroumov, V.G.; Shcherbakov, I.A. 2.79 μm YSGG:Cr:Er Laser pumped at 790 nm. *IEEE J. Quantum Electron.* **1994**, *30*, 2608–2611. [[CrossRef](#)]
43. Vodopyanov, K.L.; Ganikhanov, F.; Maffetone, J.P.; Zwieback, I.; Ruderman, W. ZnGeP₂ optical parametric oscillator with 3.8–12.4 μm tunability. *Opt. Lett.* **2000**, *25*, 841–843. [[CrossRef](#)] [[PubMed](#)]
44. Diening, A.; Kuck, S. Spectroscopy and diode-pumped laser oscillation of Yb³⁺, Ho³⁺-doped yttrium scandium gallium garnet. *J. Appl. Phys.* **2000**, *87*, 4063–4068. [[CrossRef](#)]
45. Dou, R.; Zhang, Q.; Liu, W.; Luo, J.; Wang, X.; Ding, S.; Sun, D. Growth, structure, chemical etching, and spectroscopic properties of a 2.9 μm Tm,Ho:GdYTaO₄ laser crystal. *Opt. Mater.* **2015**, *48*, 80–85. [[CrossRef](#)]
46. Dou, R.; Zhang, Q.; Sun, D.; Luo, J.; Yang, H.; Liu, W.; Sun, G. Growth, thermal, and spectroscopic properties of a 2.911 μm Yb,Ho:GdYTaO₄ laser crystal. *CrystEngComm* **2014**, *16*, 11007–11012. [[CrossRef](#)]
47. Chen, D.W.; Fincher, C.L.; Rose, T.S.; Vernon, F.L.; Fields, R.A. Diode-pumped 1-W continuous-wave Er:YAG 3 μm laser. *Opt. Lett.* **1999**, *24*, 385–387. [[CrossRef](#)] [[PubMed](#)]
48. Deloach, L.D.; Payne, S.A.; Smith, L.K.; Kway, W.L.; Krupke, W.F. Laser And Spectroscopic Properties of Sr₅(PO₄)₃F:Yb. *J. Opt. Soc. Am. B* **1994**, *11*, 269–276. [[CrossRef](#)]
49. Boulon, G.; Collombet, A.; Brenier, A.; Cohen-Adad, M.-T.; Yoshikawa, A.; Lebbou, K.; Lee, J.H.; Fukuda, T. Structural and spectroscopic characterization of nominal Yb³⁺:Ca₈La₂(PO₄)₆O₂ oxyapatite single crystal fibers grown by the micro-pulling-down method. *Adv. Funct. Mater.* **2001**, *11*, 263–270. [[CrossRef](#)]
50. Ding, S.; Zhang, Q.; Luo, J.; Liu, W.; Lu, W.; Xu, J.; Sun, G.; Sun, D. Crystal growth, structure, defects, mechanical and spectral properties of Nd_{0.01}:Gd_{0.89}La_{0.1}NbO₄ mixed crystal. *Appl. Phys. A* **2017**, *123*, 636. [[CrossRef](#)]
51. Ding, S.; Peng, F.; Zhang, Q.; Luo, J.; Liu, W.; Sun, D.; Dou, R.; Sun, G. Structure, spectroscopic properties and laser performance of Nd:YNbO₄ at 1066 nm. *Opt. Mater.* **2016**, *62*, 7–11. [[CrossRef](#)]
52. Ding, S.; Peng, F.; Zhang, Q.; Luo, J.; Liu, W.; Sun, D.; Dou, R.; Gao, J.; Sun, G.; Cheng, M. Crystal growth, spectral properties, and continuous wave laser operation of Nd:GdNbO₄. *J. Alloy. Compd.* **2017**, *693*, 339–343. [[CrossRef](#)]
53. Ding, S.; Zhang, Q.; Peng, F.; Liu, W.; Luo, J.; Dou, R.; Sun, G.; Wang, X.; Sun, D. Crystal growth, spectral properties and continuous wave laser operation of new mixed Nd:GdYNbO₄ laser crystal. *J. Alloy. Compd.* **2017**, *698*, 59–63. [[CrossRef](#)]
54. Rosen, A.; Ellis, D.E. Relativistic Molecular Calculations in Dirac-Slater Model. *J. Chem. Phys.* **1975**, *62*, 3039–3049. [[CrossRef](#)]
55. Van Pieterse, L.; Reid, M.F.; Wegh, R.T.; Soverna, S.; Meijerink, A. 4fⁿ → 4fⁿ⁻¹5d transitions of the light lanthanides: Experiment and theory. *Phys. Rev. B* **2002**, *65*, 045113. [[CrossRef](#)]
56. Reid, M.F.; Duan, C.-K.; Zhou, H. Crystal-field parameters from ab initio calculations. *J. Alloy. Compd.* **2009**, *488*, 591–594. [[CrossRef](#)]
57. Molina, P.; Loro, H.; Álvarez-García, S.; Bausá, L.E.; Rodríguez, E.M.; Guillot-Noël, O.; Goldner, P.; Bettinelli, M.; Ghigna, P.; Solé, J.G. Site location and crystal field of Nd³⁺ ions in congruent strontium barium niobate. *Phys. Rev. B* **2009**, *80*, 054111. [[CrossRef](#)]

58. Loro, H.; Vasquez, D.; Camarillo, G.E.; del Castillo, H.; Camarillo, I.; Muñoz, G.; Flores, J.C.; Hernández, A.J.; Murrieta, S.H. Experimental study and crystal-field modeling of Nd³⁺ 4f³ energy levels in Bi₄Ge₃O₁₂ and Bi₄Si₃O₁₂. *Phys. Rev. B* **2007**, *75*, 125405. [[CrossRef](#)]
59. Dagama, A.A.S.; Desa, G.F.; Porcher, P.; Caro, P. Energy-Levels of Nd³⁺ in LiYF₄. *J. Chem. Phys.* **1981**, *75*, 2583–2587. [[CrossRef](#)]
60. Duan, C.-K.; Tanner, P.A.; Makhov, V.N.; Kirm, M. Vacuum ultraviolet spectra and crystal field analysis of YAlO₃ doped with Nd³⁺ and Er³⁺. *Phys. Rev. B* **2007**, *75*, 195130. [[CrossRef](#)]



© 2018 by the authors. Licensee MDPI, Basel, Switzerland. This article is an open access article distributed under the terms and conditions of the Creative Commons Attribution (CC BY) license (<http://creativecommons.org/licenses/by/4.0/>).